Computer Methods in Applied Mechanics and Engineering 199 (2010) 2544–2558

Contents lists available at ScienceDirect

Computer Methods in Applied Mechanics and Engineering

journal homepage: www.elsevier.com/locate/cma

A new shock-capturing technique based on Moving Least Squares for higher-order numerical schemes on unstructured grids

X. Nogueira [a], L. Cueto-Felgueroso [b], I. Colominas [a,*], F. Navarrina [a], M. Casteleiro [a]

[a] Group of Numerical Methods in Engineering, Dept. of Applied Mathematics, Universidade da Coruña, Campus de Elviña, 15071, A Coruña, Spain
[b] Dept. of Civil and Environmental Engineering, Massachusetts Institute of Technology, 77 Massachusetts Ave, Cambridge, MA 02139, USA

ARTICLE INFO

Article history:
Received 26 August 2009
Received in revised form 9 February 2010
Accepted 13 April 2010
Available online 21 April 2010

Keywords:
High-order methods
Shock detection
Moving Least Squares
Slope limiters
Unstructured grids

ABSTRACT

This paper presents a shock detection technique based on Moving Least Squares reproducing kernel approximations. The multiresolution properties of these kinds of approximations allow us to define a wavelet function to act as a smoothness indicator. This MLS sensor is used to detect the shock waves. When the MLS sensor is used in a finite volume framework in combination with slope limiters, it improves the results obtained with the single application of a slope-limiter algorithm. The slope-limiter algorithm is activated only at points where the MLS sensor detects a shock. This procedure results in a decrease of the artificial dissipation introduced by the whole numerical scheme. Thus, this new MLS sensor extends the application of slope limiters to higher-order methods. Moreover, as Moving Least Squares approximations can handle scattered data accurately, the use of the proposed methodology on unstructured grids is straightforward. The results are very promising, and comparable to those of essentially non-oscillatory (ENO) and weighted ENO (WENO) schemes. Another advantage of the proposed methodology is its multidimensional character, that results in a very accurate detection of the shock position in multidimensional flows.

1. Introduction

As it is known, the use of high-order numerical methods for the resolution of compressible flows on unstructured grids is a very complex problem, due to the conflict between keeping the high accuracy and the stabilization the computations.

Among all the possible techniques to deal with this kind of flows we can cite Total Variation Diminishing (TVD) methods, essentially non-oscillatory (ENO) and weighted ENO (WENO) schemes. Another different approach is given by shock fitting techniques and multiresolution methods.

TVD schemes [19,34,59,63] and artificial viscosity methods [34,59] are based on the same principle: the addition of extra dissipation to avoid the spurious oscillations near strong gradients. Two of the most popular TVD techniques are flux-limiter methods and slope-limiter methods. Flux-limiter methods [51,61,65] are based on the development of a single numerical flux from two different fluxes. One of them (F_l) works well in smooth regions of the flow, and the other one (F_h) works well near discontinuities. The single flux has to match with (F_l) in smooth regions and with (F_h) near discontinuities. On the other hand, slope-limiter methods [4,31,65,67] are based on the limitation of the gradient of the Taylor reconstruction in generalized Godunov's methods. The limitation is obtained by decreasing the value of the gradient near discontinuities or extreme points.

ENO and WENO schemes [1,7,8,13,14,20,21,26,27,53–55,60,73] approach the problem in a different way. They use adaptive stencils in the reconstruction procedure based on the local smoothness of the numerical solution to achieve high accuracy avoiding oscillations near discontinuities. ENO schemes [20,21,53–55] use one stencil among all candidate stencils in each time step. WENO schemes [55] use a linear combination of the candidate stencils to obtain a higher-order approximation. Improvements of the original WENO scheme are the mapped WENO scheme [26] and the WENO-Z scheme [7]. Although ENO and WENO schemes obtain very good results when structured grids are used, their application to unstructured grids is complicated due to the difficulties for choosing the appropriate stencil. Extensive research has been performed in this field [1,8,13,14,27,60,73].

Shock capturing methods present several issues related to solution quality, particularly on unstructured grids. A lot of research has been developed to overcome these problems [17,29,72].

Shock fitting techniques [37,38,50] identify the shock as a singular line and compute the shock motion and upstream and downstream states with the Rankine Hugoniot equations. These techniques were proposed and developed in the 60s, but they were replaced by shock-capturing techniques. The above mentioned problems of shock-capturing methods on unstructured grids may make these methods competitive [43,69].

In the context of high-order numerical methods, Discontinuous Galerkin (DG) methods [5,9], have attracted the attention of

* Corresponding author.
E-mail address: icolominas@udc.es (I. Colominas).

0045-7825/$ – see front matter © 2010 Elsevier B.V. All rights reserved.
doi:10.1016/j.cma.2010.04.007

researchers during the past years. These methods present a very systematic way to increase the order of accuracy of the scheme. In order to extend the use of DG methods to compressible flows, many authors have developed techniques to solve flows with shocks by using limiters [32] or additional viscosity [44], by combining DG with ENO–WENO schemes [15] or by modifying the classical formulation of DG [36]. Recently a kind of limiters for DG based on ENO methods have been developed [46–48,74]. Unfortunately, the treatment of shocks with DG is still an open problem. When finite element methods are used to solve flow problems, the streamline-upwind/Petrov–Galerkin (SUPG) formulation for compressible flows [24,25,28,52,62] is one of the most prevalent methods.

Another technique to solve shocks is based on the multiresolution properties of the numerical schemes. Thus, the application of filters can be used to suppress the oscillations caused by shocks. This approach has been used in a finite difference framework [6,67], due to the excellent performance of numerical filters on Cartesian grids. Other kinds of filters based on the dissipative part of a shock-capturing scheme have also been used in [2,16,71].

The most usual approach on unstructured grids is to use methods based on a Taylor reconstruction of the variables with slope limiters. However, most of the existing slope limiters are only designed for second order schemes, by limiting the first derivative of the Taylor reconstruction. The straightforward application of slope limiters to higher-order schemes by limiting high-order derivatives with the same coefficients than first derivatives, may result in bad behavior of the solution. Moreover, slope limiters usually identify regions near smooth extrema as requiring limitation. As a result, the optimal higher-order convergence rate of the numerical scheme is reduced, even in the absence of shocks. In this context, Colella has developed a limiter for the Piecewise Parabolic Method (PPM) [10] that preserves accuracy at smooth extrema [11]. Another drawback of slope limiters is that they avoid the total convergence of the numerical method. This is due to the fact that even machine-order differences between neighbor cells may activate the limitation process. A possible way of improving this behavior is to develop a selective limiting method, by measuring the smoothness of the solution and switching off the limiter when the solution may be accurately resolved by the approximation scheme. With this procedure, optimal higher-order convergence rate in smooth areas can be recovered. In this context the definition of the shock detector is a crucial point and several kinds of sensors have been developed. Among others, we can cite [2,22,30,45,57]. Recently, a 1D MLS sensor based on the multiresolution properties of the Moving Least Squares (MLS) [33] approximations has been presented [12]. This procedure can be regarded as an unstructured grid generalization of the wavelet-based selective filtering proposed in [57] for finite differences. This procedure preserves the accuracy at smooth extrema for a numerical scheme with any slope-limiter and it improves the convergence of the numerical method.

In this work the extension of this technique to multidimensional problems on unstructured grids is presented and tested. Section 2 presents the fundamentals of Moving Least Squares approximations. Since the methodology of detection is based on the separation of scales, Section 3 is devoted to introduce MLS-based filters. In Section 4 the MLS-based sensor for shock detection is presented. In Section 5 we present several numerical examples in both structured and unstructured grids and for steady and unsteady flows, with the purpose of showing the performance of the proposed methodology. Finally, conclusions are drawn.

2. Moving Least Squares reproducing kernel approximations

The methodology proposed in this paper is based in the properties of the Moving Least Squares (MLS) approximations. This is a well-know numerical technique widely used in the meshless community. A complete description of the method can be found in [35]. Here, for the sake of brevity we only recall that the interpolation structure can be identified as

$$\hat{u}(\boldsymbol{x}) = \sum_{j=1}^{n_x} N_j(\boldsymbol{x}) u_j \tag{1}$$

where, in analogy to the finite element method, the approximation is written in terms of the MLS "shape functions" $\boldsymbol{N}^T(\boldsymbol{x})$. To compute these shape functions for a given point, we need to use a number of its neighboring points. The number of neighbors depends on the order of accuracy required. However, the cloud of neighbors must fulfill certain "good neighborhood" requirements. The definition of the cloud (the *MLS stencil*) for each evaluation point is a crucial issue that requires careful attention. The selection process must be suitable for general unstructured grids, and the stencil should be as compact as possible for the sake of computational efficiency and physical meaning. Note that these stencils are typically *centered* around the node, and thus the MLS approximation avoids the spatial bias which is often found in patch-based piecewise polynomial approximations. The particles needed for the application of the method are identified with the centroids of every cell of the grid, as it is shown in Fig. 1. This stencil is the one we have used in all the examples of this work. More details can be found in [12].

The MLS shape functions are data independent and, therefore, for fixed grids they need to be computed *only once* at the preprocessing phase.

In the definition of the MLS shape functions, kernel functions play a crucial role [12,35,41]. It is possible to use different kernels for the definition of shape functions. We have considered two of them: the cubic spline kernel and the exponential kernel. The 1D cubic kernel is given by:

$$W(s) = \begin{cases} 1 - \frac{3}{2}s^2 + \frac{3}{4}s^3 & s \le 1 \\ \frac{1}{4}(2-s)^3 & 1 < s \le 2 \\ 0 & s > 2 \end{cases} \tag{2}$$

In Eq. (2) $s = \frac{|x_j - x^*|}{h}$, and $h = k \max(|x_j - x^*|)$ with $j = 1,\ldots, n_{x^*}$, x^* is the reference point (the point where the MLS-shape functions are evaluated), and n_{x^*} is the number of neighbors of the reference point. Different values of k affect the behavior of the numerical scheme, and a value of k between 0.6 and 0.7 is recommended [41].

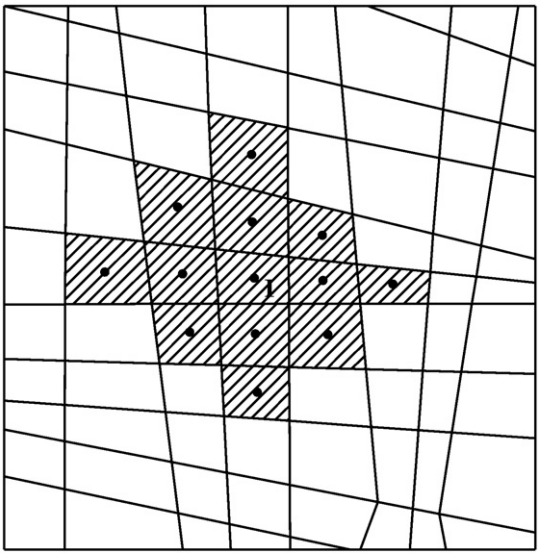

Fig. 1. 2D stencil for the MLS reconstruction in interior cells.

The exponential kernel may be defined in 1D as:

$$W(x,x^*,\kappa_x) = \frac{e^{-\left(\frac{s}{c}\right)^2} - e^{-\left(\frac{dm}{c}\right)^2}}{1 - e^{-\left(\frac{dm}{c}\right)^2}} \tag{3}$$

with $s = |x_j - x^*|$, $d_m = \max(|x_j - x^*|)$, with $j = 1,\ldots,n_{x^*}$, $c = \frac{d_m}{2\kappa_x}$, x is the position of every cell centroid of the stencil, x^* is the reference point and κ_x is a shape parameter. A typical value for this parameter is $\kappa = 1$ (see [41]). A 2D kernel is obtained by multiplying two 1D kernels. Thus, the 2D exponential kernel is the following:

$$W_j\left(\boldsymbol{x},\boldsymbol{x}^*,\kappa_x,\kappa_y\right) = W_j(x,x^*,\kappa_x)W_j\left(y,y^*,\kappa_y\right) \tag{4}$$

In this work, all the examples are computed with a higher-order finite volume scheme, namely FV-MLS method [12,39–41]. This method uses MLS approximations to compute the derivatives needed for the Taylor reconstruction of the variable of hyperbolic terms in a finite volume framework. Viscous terms of Navier–Stokes equations are directly computed at integration points. With this approach we obtain a high-order and centered discretization of the viscous terms. The methodology presented in this work is easily fitted in a MLS-based numerical scheme, but may also be used with any other numerical scheme. In that case, the additional cost introduced compared with classical slope-limiters techniques is mainly the computation of MLS-shape functions. We remark that for fixed grids this computation is performed only at the beginning of the computations as a part of the preprocess. Thus, the additional cost introduced is very low.

Since the MLS sensor presented in this work is based in the separation of the high-frequency content of the solution, it is worth to start with a brief exposition of MLS filtering.

3. MLS-based filters

The development of explicit numerical filters has attracted the attention of researchers of the field of turbulence, particularly in the case of Large-Eddy simulation (LES). LES methodology needs a separation between the different scales of the flow, and this separation may be performed with explicit numerical filters. The use of the *Reproducing Kernel Particle Method* (RKPM)) as a filter for turbulence problems was proposed in [68]. Thus, a MLS approximation of a variable can be seen as a low-pass filtering of the variable. Following Eq. (1) we write for a given variable Φ:

$$\overline{\Phi_I} = \sum_{j=1}^{n} N_j(\boldsymbol{x})\Phi_j \tag{5}$$

where n is the number of neighbors of the *stencil* of cell I, and we use the notation $\bar{}$ to indicate a filtered variable.

The filter properties are analyzed by the study of its transfer function, that is, a mathematical model that indicates the answer of a system for a certain input. In this case, the input is the nodal value of the variable. The answer is the result of applying a MLS approximation to the nodal values of the variable. Then, the transfer function associated to Eq. (5) is:

$$\hat{G}(\kappa) = \sum_{j=1}^{n} N_j(\boldsymbol{x})e^{i\kappa\left(x_j - x_I\right)} \tag{6}$$

$\hat{G}(\kappa)$ is determined by the number of points of the stencil, the kind of basis and the kernel function used to build the MLS shape functions.

In Fig. 2 we plot the transfer function of MLS filters with kernels Eqs. (2) and (3) for different values of its parameters. In that figure, a value of $\hat{G} = 1$ indicates no filtering. We note that we can vary the properties of the MLS-based filter by modifying the shape parameter κ for the exponential kernel or the k parameter in case of the cubic spline. This is the basis of the proposed MLS-based sensor.

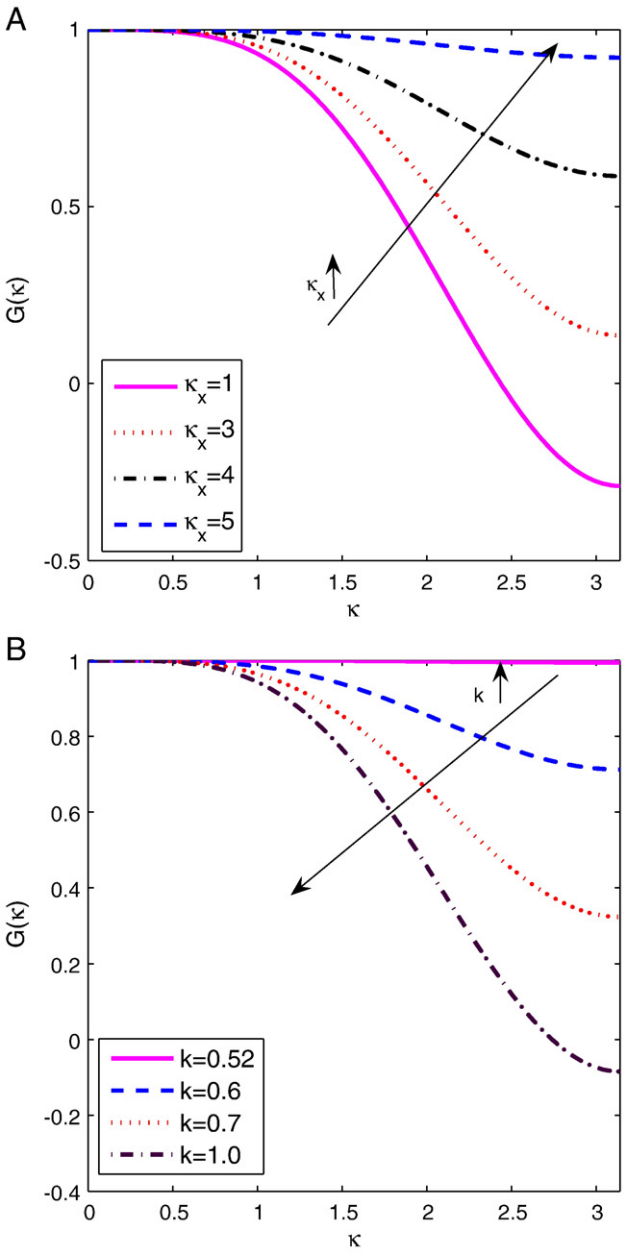

Fig. 2. 1D transfer function of the exponential kernel (A), and cubic spline kernel (B).

4. MLS-based shock detection method

Slope-limiters are a usual technique to build TVD methods. It is commonly used with second-order finite volume schemes. In order to keep the stability of the numerical scheme when the flow is not smooth, a slope-limiter limits the Taylor reconstruction of a high-order finite volume scheme as follows:

$$\boldsymbol{U}(\boldsymbol{x}) = \boldsymbol{U}_I + \chi_I \nabla \boldsymbol{U}_I \cdot (\boldsymbol{x} - \boldsymbol{x}_I) \tag{7}$$

χ_I is a parameter between 0 and 1 computed with some slope-limiter algorithm. A straightforward extension to higher-order Taylor

reconstructions is to use the same value of χ_I to limit all the derivatives:

$$\boldsymbol{U}(\boldsymbol{x}) = \boldsymbol{U}_I + \chi_I(\nabla \boldsymbol{U}_I \cdot (\boldsymbol{x}-\boldsymbol{x}_I) + \ldots) \tag{8}$$

However, slope-limiters are developed for second-order schemes and this straightforward extension to higher-order schemes presents problems. Then, the use of a higher-order scheme with slope limiters does not guarantee a more accurate solution. Thus, we need to introduce improvements in the limitation technique, in order to use slope limiters with higher-order methods efficiently. A possible methodology is selective limiting, that is, we only use the slope-limiter in those points where necessary. Even though slope limiters algorithms have some kind of detection, they are not very accurate and machine-error differences of the variable between cells can activate the slope-limiter. As a result, the order of the numerical scheme is not optimal even in smooth flows.

An efficient selective limiting procedure requires the development of more accurate techniques of detection. The detector must be able to detect strong gradients and decide if the slope-limiter must be applied at a certain point. That is, the detector is a *smoothness* indicator. Such an indicator can be developed by using the multiresolution properties of MLS shape functions. An interesting property of Reproducing Kernel methods is its connection with wavelets [35]. Wavelets are defined by a wavelet function and a scale function. Thus, it is possible to define a wavelet function from MLS shape functions.

A MLS approximation reads:

$$u^h(\boldsymbol{x}) = \sum_{j=1}^{n_I} u_j N_j^h(\boldsymbol{x}) \tag{9}$$

The approximated solution $u^h(\boldsymbol{x})$ keeps all the resolutions and properties of the solution $u(\boldsymbol{x})$, up to scale h (smoothing length). It is possible to think in MLS shape functions as the h-scale function of a wavelet, where h is the scale parameter. We recall that the value of h depends on the value of the kernel parameter k (see Eq. (2)). From the Fig. 2 we observe that a smaller value of h involves a finer-scale solution. In the following, we show how to obtain a wavelet function from MLS shape functions.

Let's consider a function $u(\boldsymbol{x})$, and let's define two sets of MLS shape functions $\boldsymbol{N}^h(\boldsymbol{x})$ and $\boldsymbol{N}^{2h}(\boldsymbol{x})$, computed with different smoothing lengths h and $2h$ (or two different shape parameters κ_x). Thus, we obtain an h-approximation and a $2h$-approximation (or a κ_H-scale and κ_L-scale, where the index H means high resolution and index L means low resolution). In the following, we continue the exposition with the κ_H-scale and κ_L-scale notation, and the scale parameter is κ.

MLS reconstructions with a different level of resolution of $\boldsymbol{U}$ read as:

$$\boldsymbol{U}^{\kappa_H}(\boldsymbol{x}) = \sum_{j=1}^{n_I} \boldsymbol{U}_j N_j^{\kappa_H}(\boldsymbol{x}), \qquad \boldsymbol{U}^{\kappa_L}(\boldsymbol{x}) = \sum_{j=1}^{n_I} \boldsymbol{U}_j N_j^{\kappa_L}(\boldsymbol{x}) \tag{10}$$

we remark that κ_H-scale and κ_L-scale approximations correspond to the high and low-resolution approximations.

Then, the wavelet function can be written as:

$$\Phi(\boldsymbol{x}) = \boldsymbol{N}^{\kappa_H}(\boldsymbol{x}) - \boldsymbol{N}^{\kappa_L}(\boldsymbol{x}) \tag{11}$$

On the other hand, κ_H-scale solution may be expressed as the sum of its low-scale ($\boldsymbol{U}^{\kappa_L}(\boldsymbol{x})$) and high-scale ($\boldsymbol{\Psi}(\boldsymbol{x})$) complementary parts, as

$$\boldsymbol{U}^{\kappa_H}(\boldsymbol{x}) = \boldsymbol{U}^{\kappa_L}(\boldsymbol{x}) + \boldsymbol{\Psi}(\boldsymbol{x}) \tag{12}$$

with

$$\boldsymbol{\Psi}(\boldsymbol{x}) = \sum_{j=1}^{n_I} \boldsymbol{U}_j \Phi_j(\boldsymbol{x}) = \sum_{j=1}^{n_I} \boldsymbol{U}_j (\boldsymbol{N}^{\kappa_H}(\boldsymbol{x}) - \boldsymbol{N}^{\kappa_L}(\boldsymbol{x})) \tag{13}$$

The low-scale $\boldsymbol{U}^{\kappa_L}(\boldsymbol{x})$ can be further decomposed using the same rationale.

Function $\boldsymbol{\Psi}(\boldsymbol{x})$ is a smoothness indicator of $U(\boldsymbol{x})$. If the value of $\boldsymbol{\Psi}(\boldsymbol{x})$ in a cell is greater than a threshold value, the limiter is activated, but it remains deactivated in the rest of the cells. We use the function $\boldsymbol{\Psi}(\boldsymbol{x})$ as a sensor to detect shock waves.

This procedure can be regarded as an unstructured grid generalization of the wavelet-based selective filtering proposed by Sjögreen and Yee for finite differences [57]. In fact, Eq. (13) is a high-pass filtering.

As a practical note, typical values for the filter length are $k = 0.7$ for the computation of the $\boldsymbol{N}^h(\boldsymbol{x})$ MLS shape functions if the cubic kernel is used and $\kappa_L = 1$ and $\kappa_H = 6$ for the exponential kernel.

However, to complete the methodology we need to define the value of $\boldsymbol{\Psi}(\boldsymbol{x})$ for which we consider the solution as non-smooth and the slope-limiter has to be activated. Thus, it is needed to define the *threshold value* of the MLS sensor from which the limiter is switched on. Several choices are available in the literature [6,45]. Following [45] we consider here the density as the reference variable, but it is possible to use the same procedure for the rest of variables. Then, we define the threshold value from the gradient of the reference variable in cell I.

$$T_v = C_{lc} |\nabla \rho| I(A_I)^{\frac{1}{d}} / M \tag{14}$$

A_I is the size (area in 2D) of the control volume I, d is the number of dimensions of the problem, C_{lc} is a parameter, and M is the free stream Mach number. If $C_{lc} = 0$, there is no selective limiting, and the usual slope-limiter algorithm is used in the whole domain of computation. We have included a Mach number scaling in order to reduce the variability of the C_{lc} parameter. This scaling reduces the problem dependency of the MLS sensor, but in general it is problem dependent. In our experience, a good initial guess is $C_{lc} = 0.32$. Note that it is also possible to use a local Mach number instead the free-stream Mach number for the scaling.

Thus, the slope-limiter algorithm is activated when the following condition is verified:

$$|\Psi_\rho| = \left| \sum_{j=1}^{n_I} \rho_j \left(N_j^{\kappa_H}(\boldsymbol{x}) - N_j^{\kappa_L}(\boldsymbol{x}) \right) \right| > T_v \tag{15}$$

The effect of selective limiting is shown in Fig. 3, where we plot the effect of the variation in the parameter C_{lc} on the dispersion properties of the third-order FV-MLS scheme [41]. The aim of this figure is to show the behavior of selective-limiting and not describing the behavior of the scheme in the resolution of multidimensional Euler equations. It is obtained for the approximation of the derivative of $u = \sin((2\pi, w x)/L)$. As we vary w, higher frequencies have to be solved. We compute the Ψ function as $\Psi = \sum_{j=1}^{n_I} u_j \left(N_j^{\kappa_H}(\boldsymbol{x}) - N_j^{\kappa_L}(\boldsymbol{x}) \right)$. When $|\Psi|$ is bigger than the threshold value defined for the variable u, the limiter is activated. We have used the slope-limiter developed by Barth and Jespersen [4], but any other slope-limiter may be used. It is observed that the effect of the slope-limiter is to transform the dispersion properties of the numerical scheme in those of a lower order scheme. It is also observed that a smaller value of the C_{lc} parameter results in an activation of the limiter for lower wavenumbers. Thus, $C_{lc} = 0$ is equivalent to keeping the slope-limiter always active.

We note that in the proposed detection algorithm, we use all the cells of the stencil to determine if a shock is present in the flow. This fact gives our approach a multidimensional nature that we believe

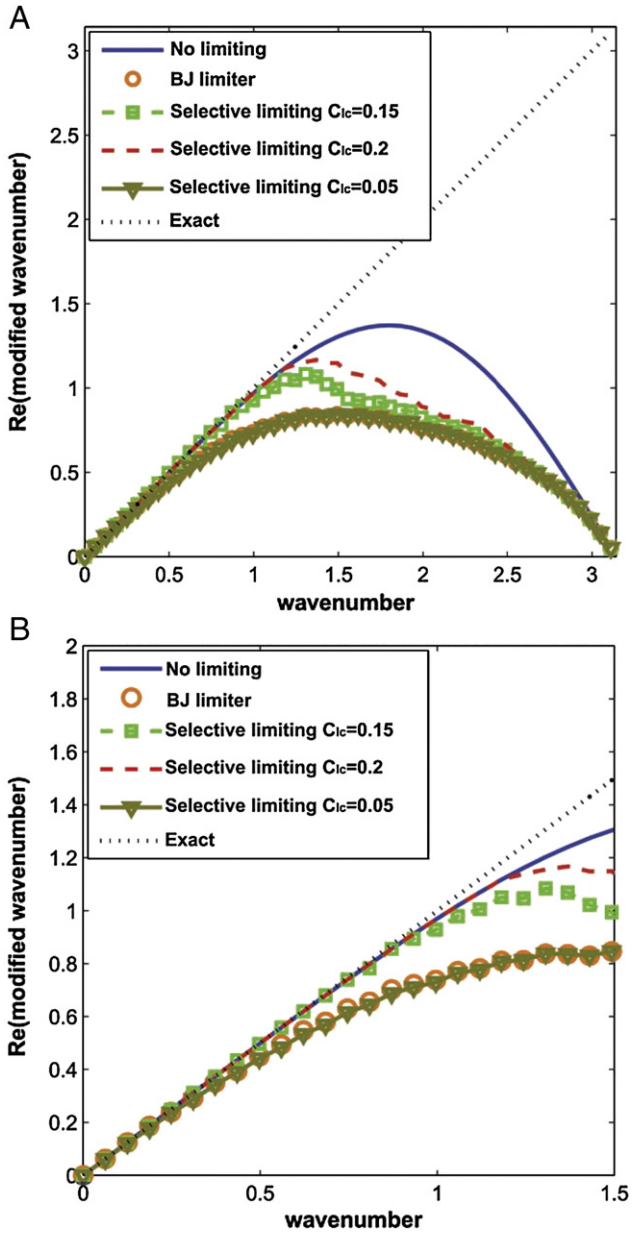

Fig. 3. Dispersion of the third-order FVMLS scheme with selective limiting for different values of C_{lc} parameter. On the top we show the result with the threshold value defined from the gradient of the reference variable in cell *I*. On the bottom, we plot a zoom of the curve. BJ-limiter refers to Barth and Jespersen limiter [4].

improve the accuracy in the detection of shocks for multidimensional flows. We also note that the methodology proposed here improves the way of detecting the shock of a given slope-limiter technique. However, once the limiter is active, the process of limiting is the same than the one of the original limiter.

4.1. Detection tests

In this section we check the ability of the proposed methodology to detect the discontinuities in a 2D data distribution. Data distribution is built from the Abgrall function [1,42]:

$$u(x,y) = \begin{cases} f\left(x - \cot\sqrt{\frac{\pi}{2}}y\right) & x \le \frac{\cos \pi y}{2} \\ f\left(x + \cot\sqrt{\frac{\pi}{2}}y + \cos(2\pi y)\right) & x > \frac{\cos \pi y}{2} \end{cases} \quad (16)$$

with

$$f(r) = \begin{cases} -r\sin\left(\frac{3\pi}{2}r^2\right) & r \le -\frac{1}{3} \\ |\sin(2\pi r)| & |r| < \frac{1}{3} \\ 2r - 1 + \frac{1}{6}\sin(3\pi r) & r \ge \frac{1}{3} \end{cases} \quad (17)$$

A plot of the Abgrall function is shown in Fig. 4.

We apply the MLS-based shock detection methodology to the function (16) on a unstructured grid. In Fig. 5 we plot the detection for different choices of the threshold value definition.

In order to guarantee the stability in general grids, we activate the slope-limiter in all the cells of the stencil of *I* when the condition given by Eq. (15) is verified in the cell *I*. The application of this methodology to the Abgrall function (16) obtains the results we plot in Fig. 6.

We note that the increase in the number of cells marked by the MLS sensor is alleviated by using the "detection" algorithm of each slope limiter in addition to our proposed MLS-sensor. Thus, although the slope-limiter is active it does not mean that $\chi_I = 0$, because once a cell has been marked by the MLS sensor the slope limiter decides if this cell is limited or not, and the amount of limiting to perform.

The multidimensional nature and multiresolution features of the Moving Least Squares approximations allow a very accurate detection of the position of the discontinuity. In the following section, this will be further shown with several representative simulations.

5. Representative simulations

5.1. 1D test. Shu–Osher problem

As a first example, we consider the test number 8 of the 1D problems that Shu and Osher presented in [56]. We solve the 1D Euler equations in $[-5, 5]$, with 400 cells. Initial conditions are $(\rho, v, p) = (3.857, 2.629, 10.333)$ if $x < -4$ and $(\rho, v, p) = (1 + 0.2\sin(5x), 0, 1)$ if $x \ge -4$. The density ρ is the reference variable for the selective limiting procedure. We use the Barth and Jespersen slope-limiter with and without selective limiting, with a parameter $C_{lc} = 0.32$, and a Mach number value corresponding to the state 1.

In Fig. 7 we plot the results for the density. The reference solution has been computed on a 3200 elements grid, with the second-order FV-MLS scheme and the slope-limiter active everywhere. We also plot the absolute value of function Ψ and the threshold value T_v.

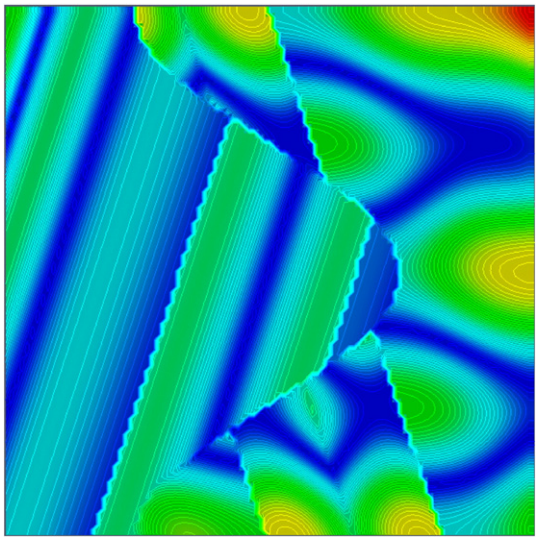

Fig. 4. Isolines of the Abgrall function given by Eq. (16).

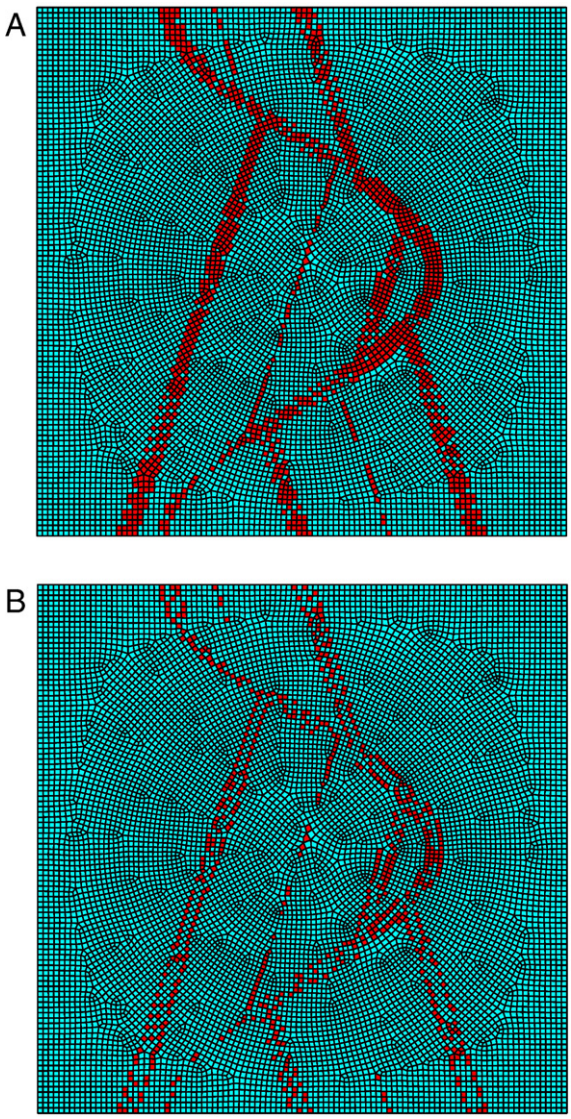

Fig. 5. Detection test for the Abgrall function (16) on an unstructured grid. We plot the results with the definition of the threshold value based on the gradient with $C_{lc}=0.2$ (left) and $C_{lc}=0.32$ (right). Marked cells are the cells where the slope-limiter algorithm would be activated. As expected, if we increase the value of C_{lc} parameter, the weaker discontinuities are progressively not detected.

The results improve considerably when the MLS sensor is applied with the slope limiter. We note that these results are comparable to those obtained with ENO and WENO schemes [56].

5.2. 2D tests. Subsonic flow past a NACA 0012 profile

One of the main drawbacks of slope limiters is the limiting in smooth regions. In these regions limiting is not needed, and the introduction of additional numerical dissipation reduces the accuracy of the numerical scheme. In this example we check this effect with the computation of a smooth flow, and we show the improvement achieved when the MLS sensor is used with the slope limiter.

We solve the Euler equations for a subsonic 2D flow past a NACA 0012 profile. Freestream Mach number is $M=0.63$ and the angle of attack is $\alpha=2°$. These flow conditions result in a smooth flow passing the profile. Drag and lift coefficients computed with the hodographic method are $C_D=0$ and $C_L=0.335$. The grid is unstructured with quadrilateral elements. We have placed 128 cells on the profile (64 on each face), and the total number of elements is 5322. The limiter of Barth and Jespersen (BJ) is used with the third order FV-MLS method.

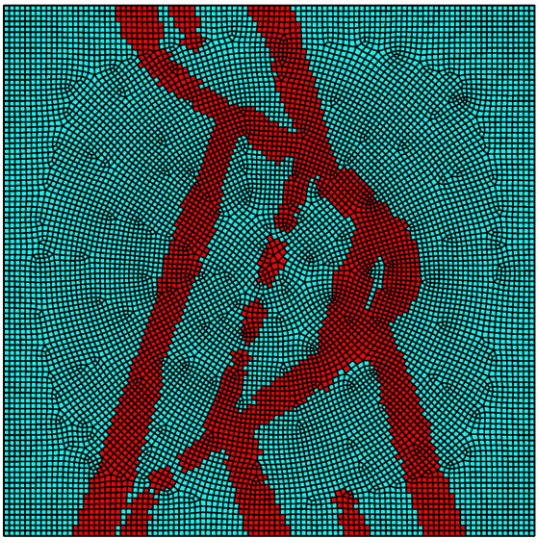

Fig. 6. Detection test for the Abgrall function (16) on an unstructured grid. We plot the result with the definition of the threshold value based on the gradient, for a value of $C_{lc}=0.32$. We mark the cells of the stencil of I when the detector activates the slope-limiter in cell I.

In Fig. 8 we show Mach isolines for the computations with and without MLS sensor with $C_{lc}=0.32$. In figure A, shaded cells indicate the cells marked by the MLS sensor, where the slope limiting algorithm is active. In figure B, colored cells are the cells where the BJ limiter is active without the MLS sensor. Color scale indicates the value of χ_I in those cells. We note that the BJ limiter is limiting although there is not any shock wave in the solution. Thus, the BJ limiter introduces an additional amount of numerical viscosity that is unnecessary, ant it causes anomalies in the Mach number lines close to the profile. When the MLS sensor is used, these anomalies disappear. Note that it is possible to reduce the number of cells marked by the MLS-sensor by increasing the value of the C_{lc} parameter.

In order to check the grid-independence of the selective-limiting procedure, we compute the same problem in a refined grid, with 12,243 control volumes, from which 256 are placed on the profile (128 on each face). We use the same parameters than in the coarser grid. The Mach lines are drawn in Fig. 9. We note that even in this refined grid, the anomalies in the Mach number close to the surface of the profile are clear when only the BJ limiter is used.

In Table 1 we show the drag and lift coefficients. The drag coefficient, C_D, is in this example an indicator of the dissipation introduced by the numerical scheme. The improvement when the MLS sensor is used is evident.

As it is known, the use of slope limiters may result in convergence problems. The limiter is active even for machine error differences between the values of the variable in adjacent cells, and it causes the impossibility of convergence under a certain value of the residual. In Fig. 10 we plot the evolution of the residual of the density. We note the improvement with the use of MLS sensor. As the MLS sensor reduces the number of cells where limiter is active, in general it obtains a better behavior of the convergence. We note that the convergence for the coarser grid when the MLS sensor is used, is better than the convergence with a finer grid without the MLS sensor.

5.3. 2D test. Transonic flow past a NACA 0012 profile

In this section we solve the 2D Euler equations for a transonic flow past a NACA 0012 profile. The freestream Mach number is $M=0.8$ and the angle of attack is $\alpha=1.25°$. We use the same grid as in the

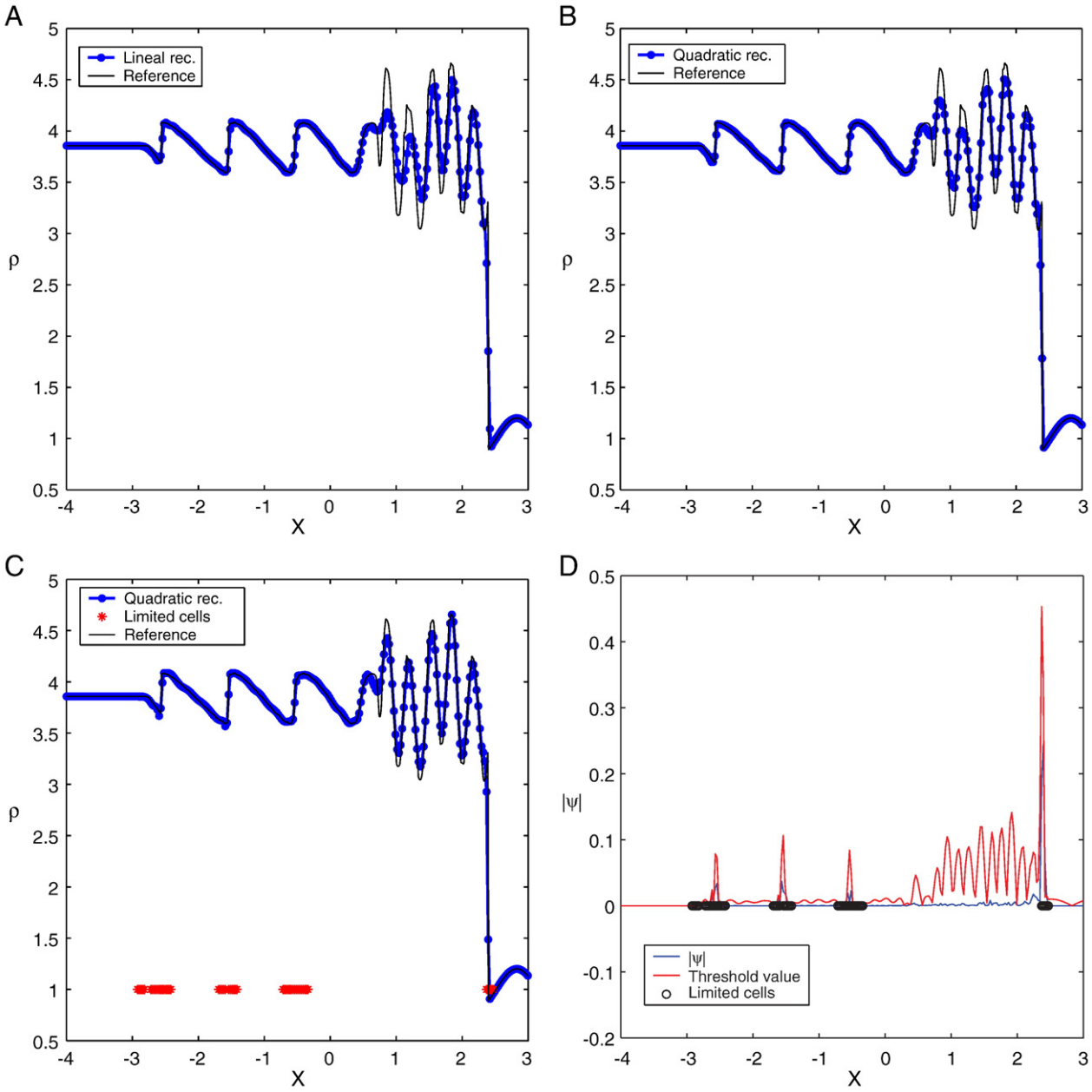

Fig. 7. Shu–Osher problem, 400 cells. (A) second-order FV-MLS scheme and limiter active everywhere, (B) third-order FV-MLS scheme and limiter active everywhere. Panel (C) shows the results for the third-order FV-MLS, BJ limiter with MLS sensor $C_{lc} = 0.32$, and in figure (D) we plot the wavelet function $|\Psi|$ and threshold value.

previous example. We have used the fourth-order FV-MLS method with the BJ limiter. When the MLS sensor is used, the value of the parameter is $C_{lc} = 0.32$.

In Fig. 11 we plot the Mach number contours and the cells where the MLS sensor detects a shock and it activates the slope-limiter (shaded cells). In these cells, the slope-limiter algorithm is applied as usual. In Fig. 12 we plot the cells where ($\chi \neq 1$), that is, the cells where the slope-limiter is limiting. A red color indicates $\chi = 0$ (a first-order scheme). A blue color indicates a value of χ close (but not equal) to one. We observe that the limiter is active in most of the surface of the profile (even in cells far from the shock) when only the BJ limiter is applied. However, when the slope-limiter is used linked with the MLS sensor, the numerical scheme does not introduce dissipation in cells far from the shock.

When the MLS sensor is used the higher-order reconstruction is recovered in cells adjacent to the wall, upstream and downstream from the shock, because the slope-limiter is not active. This effect is shown in Fig. 13, where we plot the entropy values at the cells close to the profile. Entropy generation in smooth zones of the solution may be considered as an indicator of the numerical dissipation introduced by the numerical scheme. It is clear the decreasing in the entropy with the selective limiting procedure.

On the other hand, the lift and drag coefficients are shown in Table 2. The results obtained with the MLS sensor are closer to the reference values from the *Advisory Group for Aerospace Research and Development* (AGARD) [3] in a computation on a structured grid. The lower value of drag coefficient shows the less dissipative behavior of the resulting scheme. We also note that the fourth-order method with BJ limiter without selective limiting presents a more dissipative behavior than the second-order method with BJ limiter. This is an effect of using the same value of the parameter χ_l for the limitation of high-order derivatives.

We compute the same problem with the BJ limiter and the MLS sensor on a refined grid (the same one we used in the previous case),

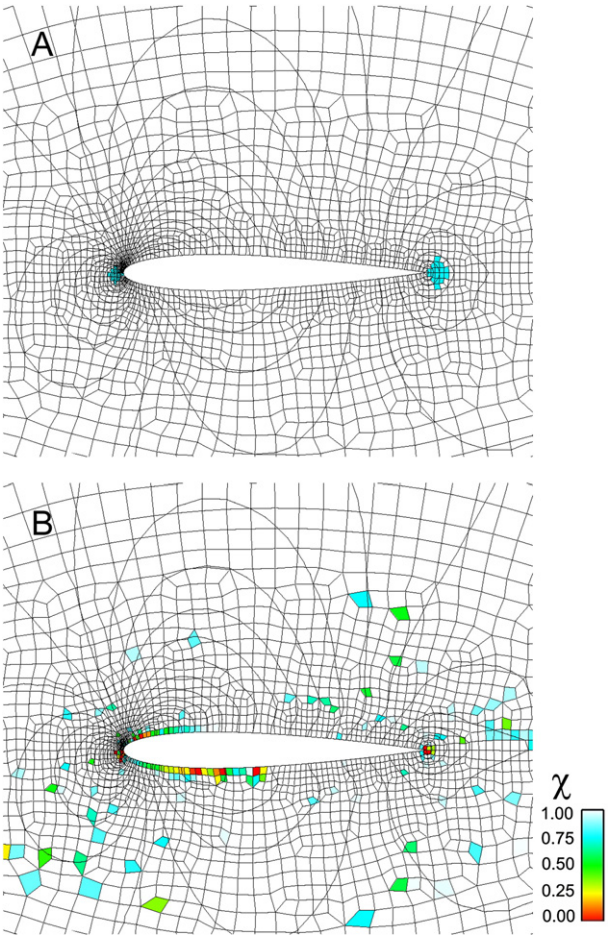

Fig. 8. Subsonic flow past a NACA 0012 profile, Mach = 0.63, $\alpha = 2$ degrees. We plot the Mach isolines for the BJ limiter with MLS sensor (A), and for the BJ limiter (B). In panel A shaded cells indicate the cells marked by the MLS sensor, where the slope limiting algorithm is active. In panel B, colored cells are the cells where the BJ limiter is active without the MLS sensor. Color scale indicates the value of χ_I in those cells. Red value is $\chi = 0$, that is, a first order scheme, and blue is χ close (but not equal) to one. Mach anomalies for the BJ limiter are clearly seen.

with the same parameters. The MLS-based selective limiting captures correctly the shocks, as it is shown in Fig. 14.

In Fig. 15 we show the pressure coefficient (C_p) for different schemes, and we compare it with a reference solution computed on the refined grid, with a second-order FV-MLS method and the BJ limiter.

5.4. 2D shock-wave–vortex interaction

In this example we show a 2D shock-wave–vortex interaction. This interaction appears in many situations, such as the flow past supersonic aircrafts. In these kinds of flows the shock–vortex interaction leads to performance deterioration. Moreover, the study of these interactions is important to predict the generation of noise [49,58].

The setup of this problem is the following, and we show it schematically in Fig. 16: a vortex is convected by a subsonic stream toward a stationary plane shock wave. When the vortex arrives, it distorts the shock wave. The distortion will depend on the relative strengths of the vortex and the shock. Following [23] we assume that the effect of Reynolds number on the physical phenomena during shock–vortex interactions is negligible, and we use the 2D Euler equations to model the problem.

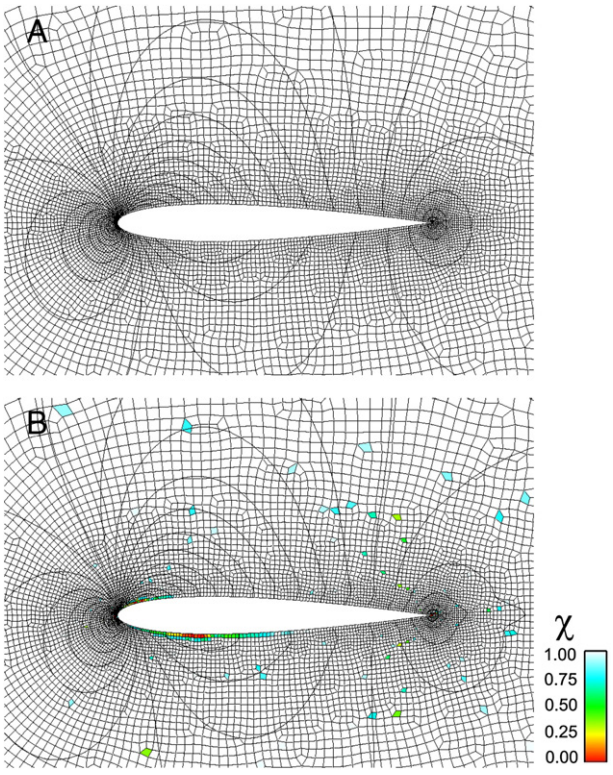

Fig. 9. Subsonic flow past a NACA 0012 profile, Mach = 0.63, $\alpha = 2°$. Results on the refined grid. We plot the Mach isolines for the BJ limiter with MLS sensor (A), and for the BJ limiter (B). In panel A shaded cells indicate the cells marked by the MLS sensor, where the slope limiting algorithm is active. In panel B, colored cells are the cells where the BJ limiter is active without the MLS sensor. Color scale indicates the value of χ_I in those cells. Red value is $\chi = 0$, that is, a first order scheme, and blue is χ close (but not equal) to one. Mach anomalies for the BJ limiter are clearly seen. Red value is $\chi = 0$, that is a first order scheme, and blue is χ close (but not equal) to one. Mach anomalies for the BJ limiter are clearly seen.

The computational domain is the rectangle $[0, 4]\times[-1, 1]$. The shock wave is plane and stationary, and it limits a supersonic region $(-)$ upstream from the shock and a subsonic region $(+)$ downstream from the shock. It is placed at $x = 0.5$.

Upstream conditions are the following:

$$\rho_s^- = 1 \tag{18}$$

$$p_s^- = 1 \tag{19}$$

$$M_s^- = 1.2 \tag{20}$$

with $M_s^- = u_s^- / \sqrt{\gamma}$. Downstream conditions are computed from the upstream conditions by writing the stationarity condition for the shock.

Table 1
Subsonic flow past a NACA 0012 profile, Mach = 0.63, $\alpha = 2°$. Drag (C_L) and lift (C_D) coefficients.

Numerical scheme	C_L	C_D
Hodographic method	0.335	0
3rd order + BJ limiter (coarse grid)	0.318	5.29E−03
3rd order + BJ limiter + MLS sensor (coarse grid)	0.328	1.24E−03
3rd order + BJ limiter (refined grid)	0.327	1.14E−03
3rd order + BJ limiter + MLS sensor(refined grid)	0.329	1.63E−04

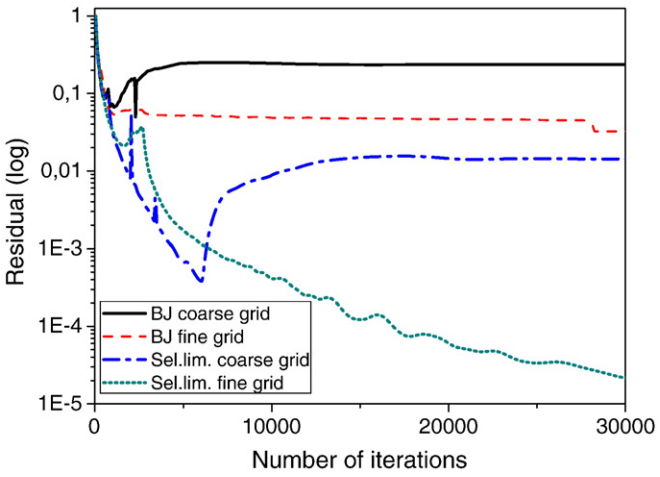

Fig. 10. Subsonic flow past a NACA 0012 profile, Mach = 0.63, $\alpha = 2$. Convergence history for the residual of the density for selective limiting and the BJ limiter.

Vortex is defined as a Taylor vortex with uniform and constant entropy:

$$u_0(x,y) = -\upsilon_{\max}\frac{y-y_{\upsilon 0}}{r_\upsilon}\exp\left(\frac{1-\xi^2}{2}\right) \tag{21}$$

$$v_0(x,y) = \upsilon_{\max}\frac{x-x_{\upsilon 0}}{r_\upsilon}\exp\left(\frac{1-\xi^2}{2}\right) \tag{22}$$

$$\rho_0(x,y) = \left[1-\frac{\gamma-1}{2}M_\upsilon^2\exp\left(1-\xi^2\right)\right]^{\frac{1}{\gamma-1}} \tag{23}$$

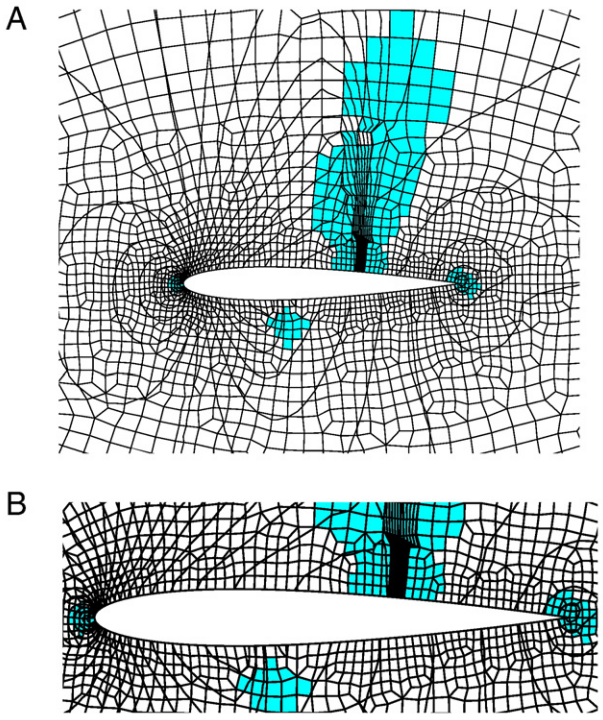

Fig. 11. Transonic flow past a NACA 0012 profile, Mach = 0.8, $\alpha = 1.25°$. Shaded cells indicate the cells where the MLS-based detector detects a shock and the slope-limiter is activated. On the bottom we plot a zoom of the profile.

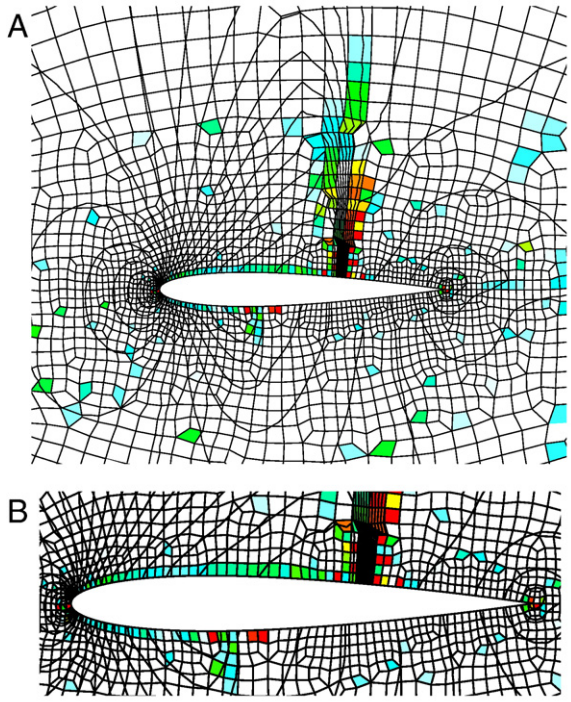

Fig. 12. Transonic flow past a NACA 0012 profile, Mach = 0.8, $\alpha = 1.25°$. We plot the cells where the BJ limiter is limiting ($\chi \neq 1$). A red value is $\chi = 0$, whereas a blue color is χ close (but not equal) to one. On the bottom we plot a zoom of the profile. We observe that with the use of the MLS-based shock detection technique, the numerical scheme does not introduce dissipation in cells far from the shock.

$$p_0(x,y) = \frac{1}{\gamma}\left[1-\frac{\gamma-1}{2}M_\upsilon^2\exp\left(1-\xi^2\right)\right]^{\frac{\gamma}{\gamma-1}} \tag{24}$$

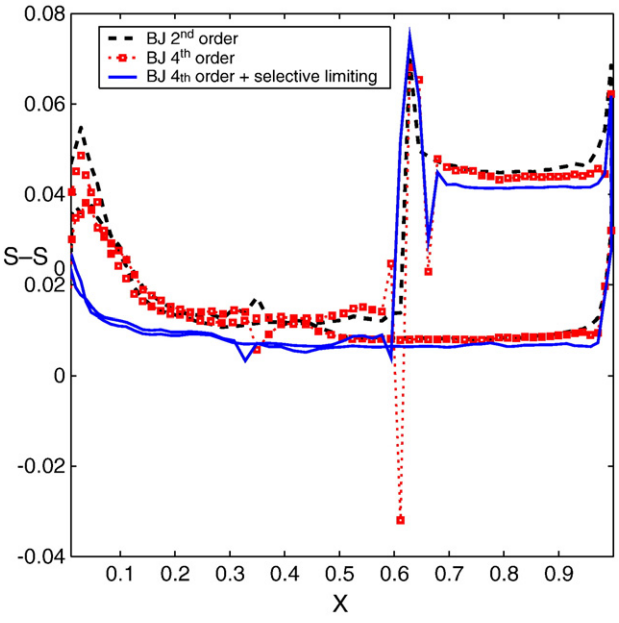

Fig. 13. Transonic flow past a NACA 0012 profile, Mach = 0.8, $\alpha = 1.25°$. Entropy generation on the surface of the profile. S_0 is the freestream entropy. Selective limiting reduces the entropy generation. The use of a fourth order scheme with BJ limiter does not decrease the generation of entropy.

Table 2
Transonic flow past a NACA 0012 profile, Mach = 0.8, $\alpha = 1.25°$. Lift (C_L) and drag (C_D) coefficients.

Numerical scheme	C_L	C_D
2nd order + BJ limiter (coarse grid)	0.341	2.465E−02
4th order + BJ limiter (coarse grid)	0.342	2.486E−02
4th order + BJ limiter + MLS sensor (coarse grid)	0.343	2.317E−02
4th order + BJ limiter + MLS sensor (refined grid)	0.349	2.24E−02
AGARD reference [3]	0.347	2.221E−02

where $\xi = \sqrt{(x-x_{v0})^2 + (y-y_{v0})^2}/r_v$. Vortex radius is $r_v = 0.075$ and the vortex is initially placed at $(x_{v0}, y_{v0}) = (0.25, 0)$. Vortex Mach number is defined as $M_v = v_{max}/c_s^- = v_{max}/\sqrt{\gamma}$, where v_{max} is the maximum rotation velocity of the vortex. It indicates the strength of the vortex and c is the speed of sound. In this example we take $M_v = 0.32$ corresponding to a moderate strength vortex.

We solve the problem on a grid with 200×200 elements, in the region $[0, 2] \times [-1, 1]$. The region $[2, 4] \times [-1, 1]$ is an absorbing layer based on grid stretching to avoid reflections on the exit of the domain

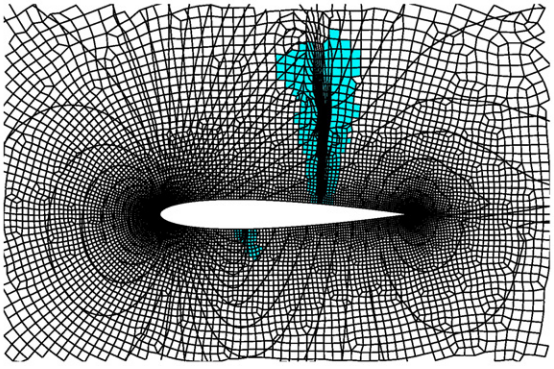

Fig. 14. Transonic flow past a NACA 0012 profile, Mach = 0.8, $\alpha = 1.25°$. Results for the refined grid. We plot the cells where the MLS sensor detects a shock and the slope-limiter is activated (shaded cells).

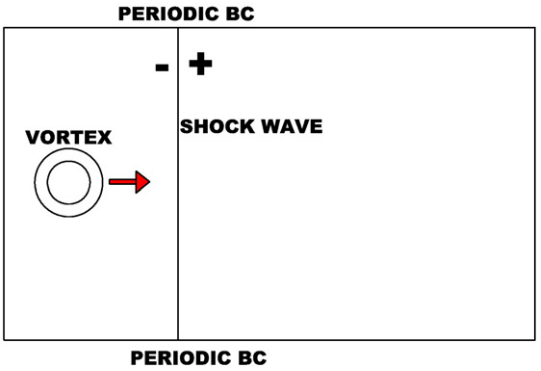

Fig. 16. Schematic representation of the 2D shock-vortex interaction.

[40]. We have used the MLS-based shock detection scheme with threshold value based on the gradient and stencil limiting. In this case, even though the value of the $C_{lc} = 0.32$ gives good results, better results are obtained with a value of coefficient is $C_{lc} = 0.48$, with a reference Mach number of 1.2.

We define the acoustic pressure fluctuation $p' = (p - p_s^+)/p_s^-$, so it is measured with respect to the undisturbed pressure level behind the shock (p_s^+) and normalized by the undisturbed pressure ahead of the shock (p_s^-). This variable allows us to analyze the sound generation produced in the shock–vortex interaction. In Fig. 17 we plot the evolution of the acoustic pressure fluctuation for several non-dimensional times $\tau = (t - t_0)c_s^+/r_v$. Non-dimensional time $\tau = 0$ corresponds to the instant when the center of the vortex goes through the shock. We note that with this definition, negative times are allowed.

With this example we show that the MLS-based shock detection methodology proposed in this paper can detect and follow the evolution of a non-stationary shock wave. Except in the cells where a shock wave is detected, the numerical scheme keeps its maximum accuracy. In Fig. 17 it is seen how the shock wave is distorted when the vortex goes through it. The detector follows the shock-wave evolution. Our results agree with the solutions obtained by other authors [6,18] with different numerical methods.

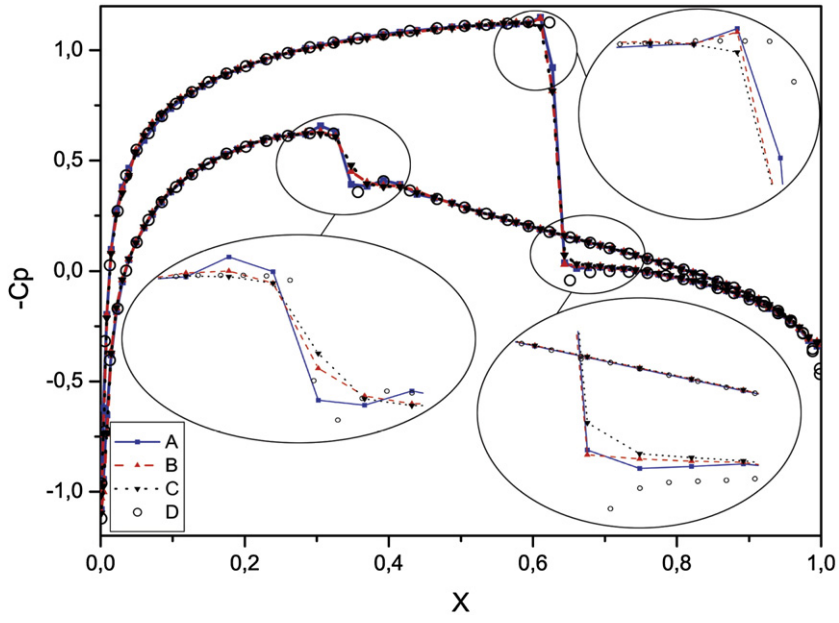

Fig. 15. Transonic flow past a NACA 0012 profile, Mach = 0.8, $\alpha = 1.25°$. Pressure coefficient for different schemes, and detail of the shock zones. (A) Fourth order FV-MLS method with selective limiting. (B) Fourth order FV-MLS method with BJ limiter. (C) Second order FV-MLS method with BJ limiter. (D) Reference solution computed with the second order FV-MLS method with BJ limiter on a refined grid. Some points of the reference solution have been skipped for clarity.

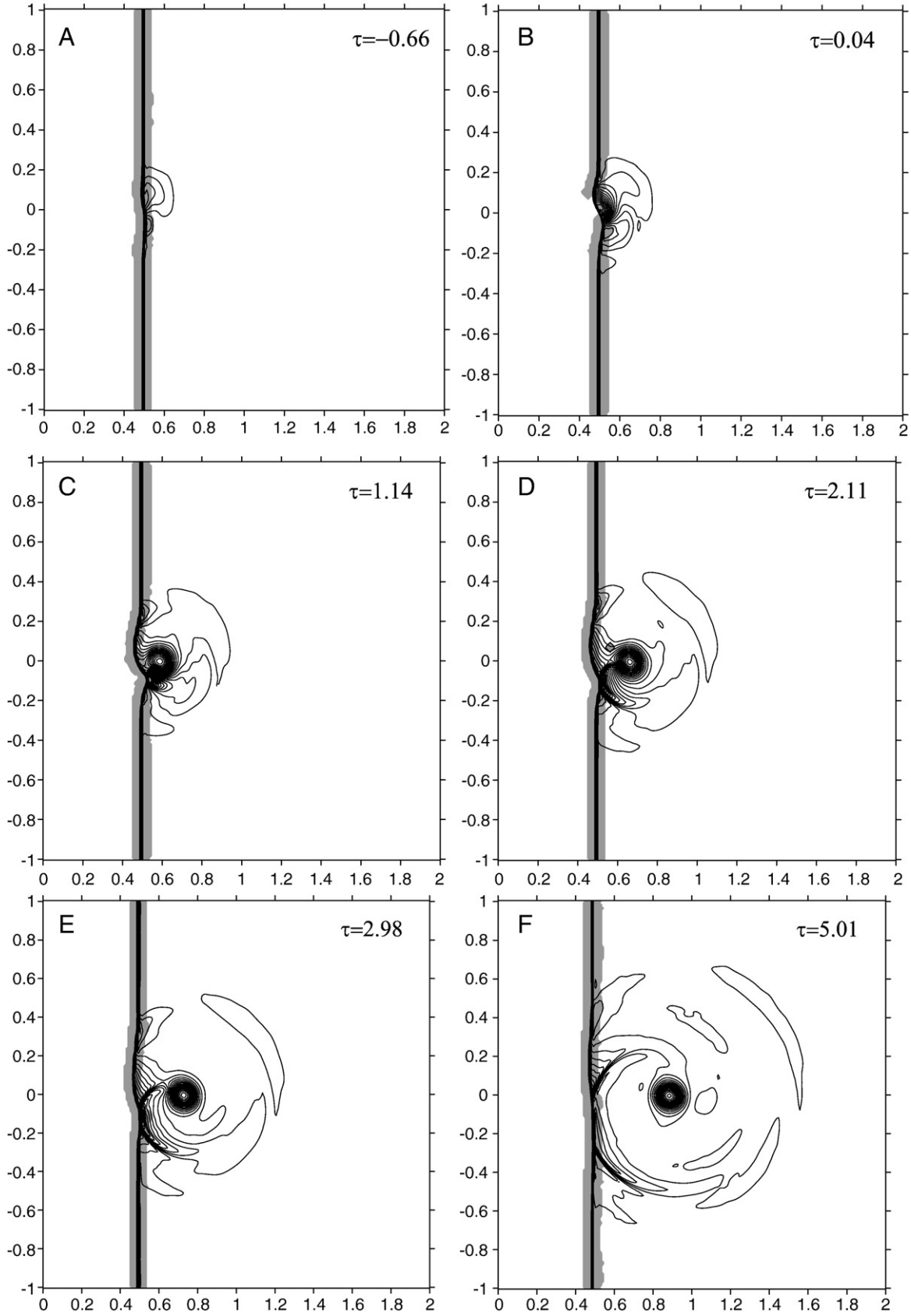

Fig. 17. 2D shock-vortex interaction. We plot the acoustic pressure fluctuation for different non-dimensional times $\tau = (t - t_0)c_s^+ / r_v$. Non-dimensional time $\tau = 0$ corresponds to the instant when the center of the vortex goes through the shock. We shade the cells in which the MLS-based sensor detects the shock. It is observed that the proposed methodology is able to follow the evolution of the shock.

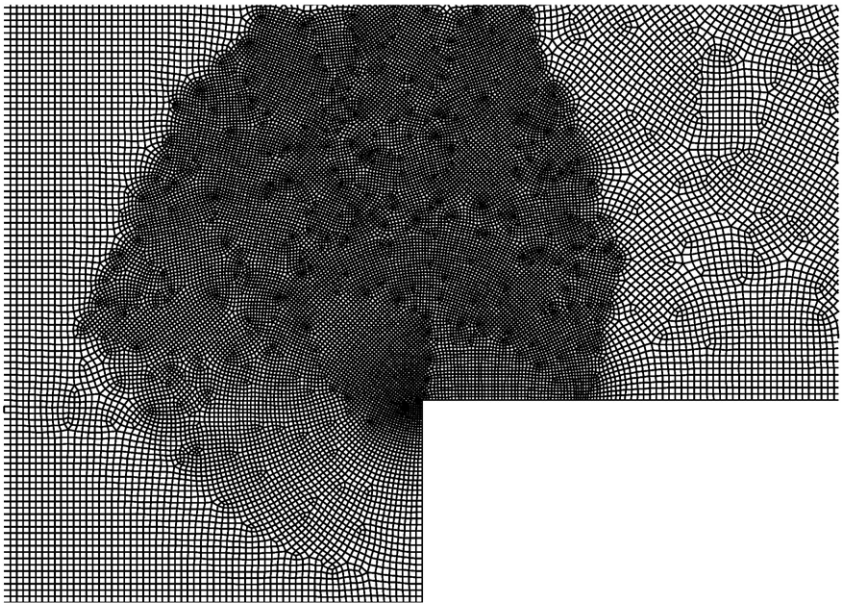

Fig. 18. Grid for the Mach 3 wind tunnel problem. Detail near the corner.

5.5. Mach 3 wind tunnel with a step

In this section we solve the problem proposed in [70]. A Mach 3 supersonic flow across a wind tunnel of 1 length unit wide and 3 length units long. A step is located 0.6 length units from the inflow, and it is 0.2 length units wide. Along the walls of the tunnel, a slip wall boundary conditions have been placed. Inflow and outflow boundary conditions are used at the entrance and the exit. We set $\rho = 1.4$, $p = 1$ as initial values of density and pressure, and the velocity is set to $v_x = 3$, $v_y = 0$. With a value of gamma $\gamma = 1.4$, this setup corresponds to a Mach 3 flow. We solve the problem with the third-order FV-MLS scheme, by using the same parameters as in previous sections. Following [27], the singularity point at the corner is managed by refining the mesh in this region. Thus, the same numerical scheme is used in the whole domain. The limiter proposed in [31] has been used in this example. The MLS sensor is used, with a parameter of $C_{lc} = 0.32$. We set the biggest size of the elements away from the corner as $\Delta x = \Delta y = \frac{1}{160}$. Size of elements near the corner is one-half that. A paving algorithm has been used to build the mesh. A detail of the grid is plotted in Fig. 18.

In Fig. 19 we plot the contours of density at time $t = 4.0$ (top), and the cells where the limiter is activated (bottom).

The results obtained agree with the results of [27] on an equivalent triangular grid. Finally, we also note that the grid used in this example is strongly non-uniform. Even on this grid the methodology is able to obtain accurate results.

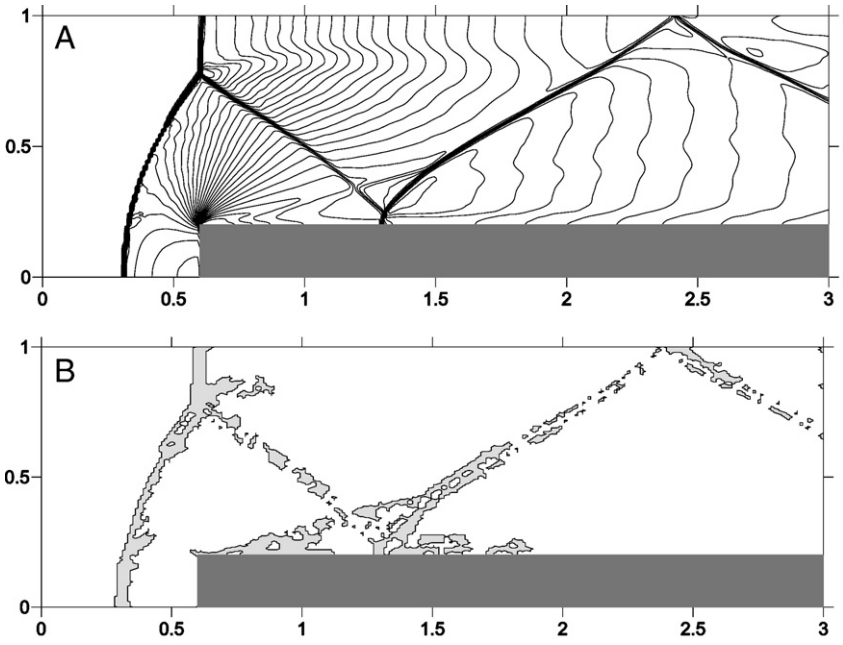

Fig. 19. Mach 3 wind tunnel problem. Density contours (top) and limited cells (bottom), $\Delta x = \Delta y = \frac{1}{160}$. We plot 30 density contours from 0.32 to 6.15 at time $t = 4.0$.

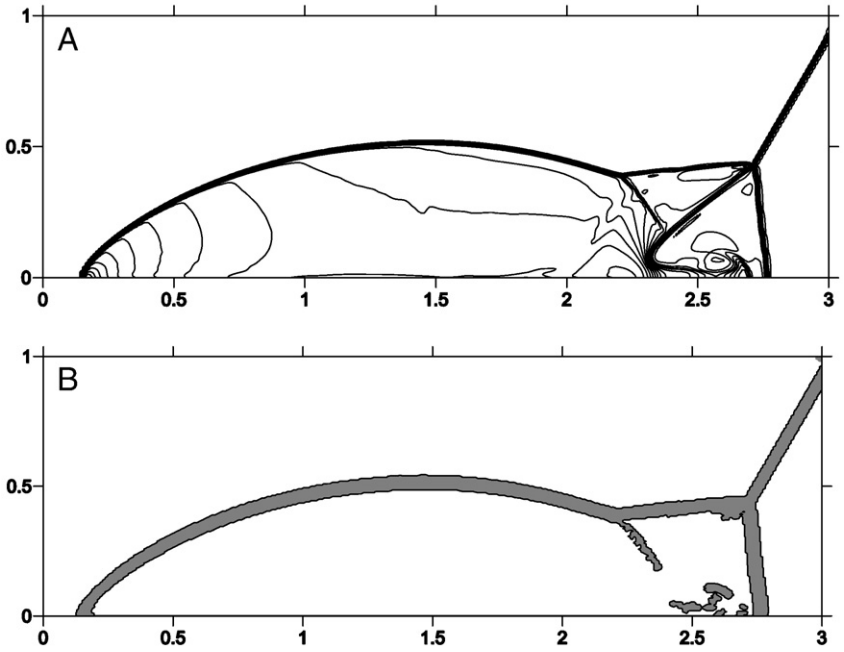

Fig. 20. Double Mach reflection. Density contours (top) and limited cells (bottom), $\Delta x = \Delta y = \frac{1}{200}$, $t = 0.2$. We plot 30 equally spaced contour lines, from 1.5 to 21.5.

5.6. Double Mach reflection

The last numerical example is the double Mach reflection problem [70]. A shock wave is moving horizontally against an edge that is inclined. This configuration is equivalent to a diagonal shock wave that moves into a reflecting wall. The domain is the rectangle $[0,4]\times[0,1]$. A Mach 10 right-moving shock is initially placed at $x_0 = \frac{1}{6}$. It is inclined 60°. The lower boundary mimics the wedge. For $x \geq x_0$ it is a reflecting wall. For $x < x_0$ we impose the exact postshock condition. At the top boundary the flow values are imposed to describe the exact motion of the inclined shock. We use the limiter of Van Albada [64] with the MLS sensor. The reference Mach number is $M = 10$. In this case a value of $C_{lc} = 0.32$ leads to an excess of marked cells and then to a very dissipative solution. Thus, we use a value of $C_{lc} = 0.5$. The size of the elements is $\Delta x = \Delta y = \frac{1}{200}$, in order to compare with the results of [27]. In Fig. 20 we plot the density contours of the region $[0, 3]\times[0, 1]$ and the limited cells for a time $t = 0.2$. We plot 30 equally spaced contour lines, from 1.5 to 21.5. It is seen that, again, the detector follows correctly the contours of the strong shock. The region of the Mach stems is almost free of limitation. The results compare very well with the results of [27] on an equivalent uniform triangular grid with a third order WENO scheme. In Fig. 21 we show a detail of the Mach stems.

6. Conclusions

A multidimensional shock detection technique based on the Moving Least Squares method that may be used in both structured and unstructured grids has been presented. Multiscale properties of MLS are used to separate the high scale components of the solution in order to develop a MLS-based wavelet function of a reference variable. This function is used as a sensor for shock waves. When the MLS sensor is bigger than a threshold the slope-limiter algorithm is switched on. The threshold value is a problem-dependent parameter. However, in our experience a value of $C_{lc} = 0.32$ is a good guess, in terms of accuracy and robustness. Moreover, this approach presents a multidimensional nature very convenient for the detection of shocks in multidimensional flows. Several numerical examples have been presented. The results obtained are comparable to those obtained by ENO and WENO schemes. However, the main interest of this new

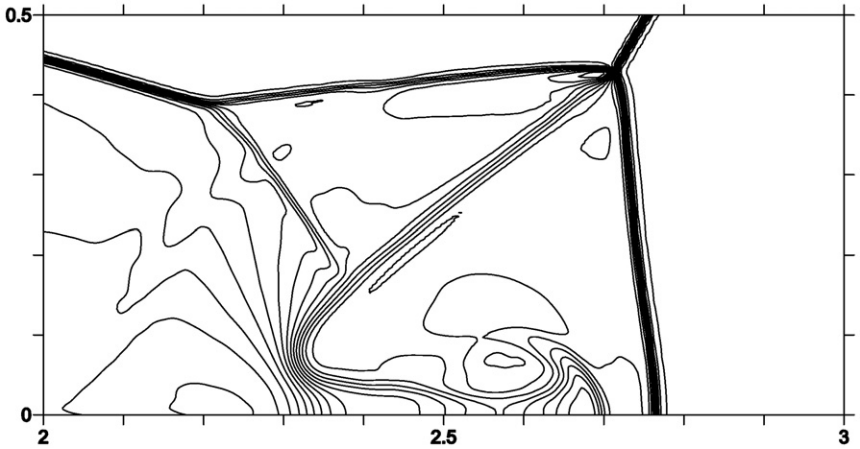

Fig. 21. Detail of the region around the double Mach stems.

technique relies on the possibility of application with unstructured grids. In those grids, the results are very promising. The proposed methodology clearly improves the results obtained by usual slope limiters by decreasing the number of cells limited. The method is robust and it allows us keeping the maximum accuracy of the scheme in smooth regions, including smooth extrema. Another important advantage of the proposed methodology is that it improves the convergence of the numerical method when slope-limiters are used.

Acknowledgments

This work has been partially supported by the *Ministerio de Educación y Ciencia* of the Spanish Government (#DPI2007-61214 and #DPI2009-14546-C02-01), cofinanced with FEDER funds and the *Secretaría Xeral de I+D* of the *Xunta de Galicia* (Grants #PGDIT09M-DS00718PR and #PGDIT09REM005118PR).

References

[1] R. Abgrall, On essentially non-oscillatory schemes on unstructured meshes: analysis and implementation, Journal of Computational Physics 114 (1994) 45–58.
[2] N.A Adams, K. Shariff, A high-resolution hybrid compact-ENO scheme for shock–turbulence interaction problems, Journal of Computational Physics 127 (1996) 27–51.
[3] AGARD AR-211, Test Cases for Inviscid Flow Fields, AGARD, 1985.
[4] T.J. Barth, D.C. Jespersen, The design and application of upwind schemes on unstructured meshes, AIAA-89-0366, 1989.
[5] F. Bassi, S. Rebay, High-order accurate discontinuous finite element solution of the 2D Euler equations, Journal of Computational Physics 138 (1997) 251–285.
[6] C. Bogey, N. de Cacqueray, C. Bailly, A shock-capturing methodology based on adaptative spatial filtering for high-order non-linear computations, Journal of Computational Physics 228 (2009) 1447–1465.
[7] R. Borges, M. Carmona, B. Costa, W.S. Don, An improved weighted essentially non-oscillatory scheme for hyperbolic conservation laws, Journal of Computational Physics 227 (6) (2008) 3101–3211.
[8] G. Capdeville, A central WENO scheme for solving hyperbolic conservation laws on non-uniform meshes, Journal of Computational Physics 227 (2008) 2977–3014.
[9] B. Cockburn, C.W. Shu, The Runge–Kutta discontinuous Galerkin method for conservation laws V: multidimensional system, Journal of Computational Physics 141 (1998) 199–224.
[10] P. Colella, P.R. Woodward, The Piecewise Parabolic Method (PPM) for gas-dynamical simulations, Journal of Computational Physics 54 (1984) 174–201.
[11] P. Colella, M.D. Sekora, A limiter for PPM that preserves accuracy at smooth extrema, Journal of Computational Physics 227 (2008) 7069–7076.
[12] L. Cueto-Felgueroso, I. Colominas, X. Nogueira, F. Navarrina, M. Casteleiro, Finite volume solvers and Moving Least-Squares approximations for the compressible Navier–Stokes equations on unstructured grids, Computer Methods in Applied Mechanics and Engineering 196 (2007) 4712–4736.
[13] M. Dumbser, M. Käser, Arbitrary high order non-oscillatory finite volume schemes on unstructured meshes for linear hyperbolic systems, Journal of Computational Physics 221 (2007) 693–723.
[14] M. Dumbser, M. Käser, V.A. Titarev, E.F. Toro, Quadrature-free non-oscillatory finite volume schemes on unstructured meshes for nonlinear hyperbolic systems, Journal of Computational Physics 226 (2007) 204–243.
[15] M. Dumbser, D.W. Balsara, E.F. Toro, C.D. Munz, A unified framework for the construction of one-step finite volume and discontinuous Galerkin schemes on unstructured meshes, Journal of Computational Physics 227 (2008) 8209–8253.
[16] E. Garnier, P. Sagaut, M. Deville, A class of explicit ENO filters with application to unsteady flows, Journal of Computational Physics 170 (2001) 184–204.
[17] J.B. Goodman, R.J. LeVeque, On the accuracy of stable schemes for 2D scalar conservation laws, Mathematics of Computation 45 (1985) 15–21.
[18] F. Grasso, S. Pirozzoli, Shock-wave–vortex interactions: shock and vortex deformations, and sound production, Theoretical and Computational Fluid Dynamics 13 (2000) 421–456.
[19] A. Harten, High resolution schemes for hyperbolic conservation laws, Journal of Computational Physics 49 (1983) 357–393.
[20] A. Harten, S. Osher, Uniformly high order accurate non-oscillatory schemes I, SIAM Journal on Numerical Analysis 24 (1987) 279–309.
[21] A. Harten, B. Engquist, S. Osher, S. Chakravarthy, Uniformly high order essentially non-oscillatory schemes III, Journal of Computational Physics 71 (1987) 231–303.
[22] A. Harten, The artificial compression method for computation of shocks and contact discontinuities. III. Self adjusting hybrid schemes, Mathematics of Computation 32 (1978) 363–389.
[23] O.M. Inoue, Y. Hattori, Sound generation by shock–vortex interactions, Journal of Fluid Mechanics 380 (1999) 81–116.
[24] G. Hauke, T.J.R. Hughes, A unified approach to compressible and incompressible flows, Computer Methods in Applied Mechanics and Engineering 113 (3–4) (1994) 389–395.
[25] A comparative study of different sets of variables for solving compressible and incompressible flows, Computer Methods in Applied Mechanics and Engineering, 153(1–2), 1–44, 1998.
[26] A.K. Henrick, T.D. Aslam, J.M. Powers, Mapped weighted essentially non-oscillatory schemes: achieving optimal order near critical points, Journal of Computational Physics 207 (2005) 542–567.
[27] C.Q. Hu, C.W. Shu, Weighted essentially non-oscillatory schemes on triangular meshes, Journal of Computational Physics 150 (1999) 97–127.
[28] T.J.R. Hughes, T.E. Tezduyar, Finite element methods for first-order hyperbolic systems with particular emphasis on the compressible Euler equations, Computer Methods in Applied Mechanics and Engineering 45 (1–3) (1984) 217–284.
[29] A. Jameson, Analysis and design of numerical schemes for gas dynamics 1 artificial diffusion, upwind biasing, limiters and their effect on accuracy and multigrid convergence, International Journal of Computational Fluid Dynamics 4 (1995) 171–218.
[30] A. Jameson, W. Schmidt, E. Turkel, Numerical solutions of the Euler equations by finite volume methods using Runge–Kutta time-stepping schemes, AIAA-81-1259, 1981.
[31] P. Jawahar, P. Kamath, A high resolution procedure for Euler and Navier–Stokes computations on unstructured grids, Journal of Computational Physics 164 (2000) 165–203.
[32] L. Krivodonova, Limiters for high-order discontinuous Galerkin methods, Journal of Computational Physics 226 (2007) 879–896.
[33] P. Lancaster, K. Salkauskas, Surfaces generated by moving least squares methods, Mathematics of Computation 37 (155) (1981) 141–158.
[34] R.J. Leveque, Numerical Methods for Conservation Laws, Birkhauser Verlag, Basel, 1990.
[35] W.K. Liu, W. Hao, Y. Chen, S. Jun, J. Gosz, Multiresolution reproducing kernel particle methods, Computational Mechanics 20 (1997) 295–309.
[36] H. Luo, J.D. Baum, R. Löhner, A discontinuous Galerkin method based on a Taylor basis for the compressible flows on arbitrary grids, Journal of Computational Physics 227 (2008) 8875–8893.
[37] G. Moretti, M. Abbett, A time-dependent computational method for blunt body flows, AIAA Journal 4 (12) (1966) 2136–2141.
[38] G. Moretti, Computation of flows with shocks, Annual Review of Fluid Mechanics 19 (1987) 313–337.
[39] X. Nogueira, L. Cueto-Felgueroso, I. Colominas, H. Gómez, F. Navarrina, M. Casteleiro, On the accuracy of finite volume and discontinuous Galerkin discretizations for compressible flow on unstructured grids, International Journal for Numerical Methods in Engineering 78 (2009) 1553–1584.
[40] X. Nogueira, I. Colominas, L. Cueto-Felgueroso, S. Khelladi, F. Navarrina, M. Casteleiro, Resolution of computational aeroacoustics problems on unstructured grids with a higher-order finite volume scheme, Journal of Computational and Applied Mathematics (in press) doi:10.1016/j.cam.2009.08.067.
[41] X. Nogueira, L. Cueto-Felgueroso, I. Colominas, S. Khelladi, On the simulation of wave propagation with a higher-order finite volume scheme based on reproducing kernel methods, Computer Methods in Applied Mechanics and Engineering 199 (2010) 1471–1490.
[42] C.F. Ollivier-Gooch, Quasi-ENO schemes for unstructured meshes based on unlimited data-dependent least-squares reconstruction, Journal of Computational Physics 133 (1997) 6–17.
[43] R. Paciorri, A. Bonfiglioli, A shock-fitting technique for 2D unstructured grids, Computers & Fluids 38 (2009) 715–726.
[44] P.O. Persson, J. Peraire, Sub-cell shock capturing for discontinuous Galerkin methods, AIAA-2006-112, January, 2006.
[45] S. Pirozzoli, Conservative hybrid compact-WENO schemes for shock–turbulence interaction, Journal of Computational Physics 178 (2002) 81–117.
[46] J. Qiu, C.W. Shu, Hermite WENO schemes and their application as limiters for Runge–Kutta Discontinuous Galerkin method: one-dimensional case, Journal of Computational Physics 193 (2003) 115–135.
[47] J. Qiu, C.W. Shu, Runge–Kutta Discontinuous Galerkin method using WENO limiters, SIAM Journal of Scientific Computing 26 (2005) 907–929.
[48] J. Qiu, C.W. Shu, A Comparison of trouble cell indicators for Runge–Kutta Discontinuous Galerkin methods using WENO limiters, SIAM Journal on Scientific Computing 27 (2005) 995–1013.
[49] A. Rault, G. Chiavassa, R. Donat, Shock–vortex interactions at high Mach numbers, Journal of Scientific Computing 19 (1–3) (2003) 347–371.
[50] R. Richtmyer, K. Morton, Difference Methods for Initial Value Problems, Interscience, New York, 1967.
[51] P.L. Roe, Some contributions to the modeling of discontinuous flows, Annual Review of Fluid Mechanics 18 (1986) 337–365.
[52] F. Shakib, T.J.R. Hughes, Z. Johan, A new finite element formulation for computational fluid dynamics: X. The compressible Euler and Navier–Stokes equations, Computer Methods in Applied Mechanics and Engineering 89 (1–3) (1991) 141–219.
[53] C.W. Shu, S. Osher, Efficient implementation of essentially non-oscillatory shock-capturing schemes, Journal of Computational Physics 77 (1988) 439–471.
[54] C.W. Shu, S. Osher, Efficient implementation of essentially non-oscillatory shock-capturing schemes II, Journal of Computational Physics 83 (1989) 32–78.
[55] C.W. Shu, Essentially non-oscillatory and weighted essentially non-oscillatory schemes for hyperbolic conservation laws, ICASE Report 97-65, 1997.
[56] C.W. Shu, S. Osher, Efficient implementation of essentially non-oscillatory shock-capturing schemes II, Journal of Computational Physics 83 (1989) 32–78.
[57] B. Sjögreen, H.C. Yee, Multiresolution wavelet based adaptive numerical dissipation control for high order methods, Journal of Scientific Computing 20 (2004) 211–255.
[58] M.K. Smart, I.M. Kalkhoran, S. Popovic, Some aspects of streamwise vortex behavior during oblique shock wave/vortex interaction, Shock Waves 8 (1998) 243–255.

[59] G.A. Sod, Numerical Methods in Fluid Dynamics, Cambridge University Press, Cambridge, 1985.
[60] T. Sonar, On the construction of essentially non-oscillatory finite volume approximations to hyperbolic conservation laws on general triangulations: polynomial recovery, accuracy and stencil selection, Computer Methods in Applied Mechanics and Engineering 140 (1997) 157–181.
[61] P.K. Sweby, High resolution schemes using flux limiters for hyperbolic conservation laws, SIAM Journal on Numerical Analysis 21 (1984) 995–1011.
[62] T.E. Tezduyar, M. Senga, Stabilization and shock-capturing parameters in SUPG formulation of compressible flows, Computer Methods in Applied Mechanics and Engineering 195 (2006) 1621–1632.
[63] E.F. Toro, Riemann Solvers and Numerical Methods for Fluid Dynamics. A Practical Introduction, Second editionSpringer Verlag, Berlin, 1999.
[64] G.D. Van Albada, B. Van Leer, W.W. Roberts, A comparative study of computational methods in cosmic gas dynamics, Astronomy and Astrophysics 108 (1982) 76–84.
[65] B. Van Leer, Towards the ultimate conservative difference scheme I. The quest of monotonicity, Springer Lecture Notes in Physics 18 (1973) 163–168.
[66] V. Venkatakrishnan, Convergence to steady state solutions of the Euler equations on unstructured grids with limiters, Journal of Computational Physics 118 (1995) 120–130.
[67] M.R. Visbal, D.V. Gaitonde, Shock capturing using compact-differencing-based methods, AIAA-2005-1265, 2005.
[68] G.J. Wagner, W.K. Liu, Turbulence simulation and multiple scale subgrid models, Computational Mechanics 25 (2000) 117–136.
[69] J.A.S. Witteveen, B. Koren, P.G. Bakker, An improved front tracking method for the Euler equations, Journal of Computational Physics 224 (2007) 712–728.
[70] P. Woodward, P. Colella, The numerical simulation of two-dimensional fluid flow with strong shocks, Journal of Computational Physics 54 (1984) 115–173.
[71] H.C. Yee, N.D. Sandham, M.J. Djomehri, Low-dissipative high-order shock-capturing methods using characteristic-based filters, Journal of Computational Physics 150 (1999) 199–238.
[72] S.H. Yoon, C. Kim, K.H. Kim, Multi-dimensional limiting process for three-dimensional flow physics analysis, Journal of Computational Physics 227 (2008) 6001–6043.
[73] Y.T. Zhang, C.W. Shu, Third order WENO scheme on three dimensional tetrahedral meshes, Communications in Computational Physics 5 (2009) 836–848.
[74] J. Zhu, J. Qiu, C.W. Shu, M. Dumbser, Runge–Kutta discontinuous Galerkin method using WENO limiters II: unstructured meshes, Journal of Computational Physics 227 (2008) 4330–4353.